ACS APPLIED MATERIALS & INTERFACES

www.acsami.org

Research Article

Improving the Optical Quality of $MoSe_2$ and WS_2 Monolayers with Complete *h*-BN Encapsulation by High-Temperature Annealing

Xiang Hua, Theodor Axenie, Mateo Navarro Goldaraz, Kyungnam Kang, Eui-Hyeok Yang, Kenji Watanabe, Takashi Taniguchi, James Hone, Bumho Kim,* and Irving P. Herman*

Cite This: *ACS Appl. Mater. Interfaces* 2022, 14, 2255−2262

Read Online

ACCESS | Metrics & More | Article Recommendations | Supporting Information

ABSTRACT: We improved the optical quality and stability of an exfoliated monolayer (ML) $MoSe_2$ and chemical vapor deposition (CVD)-grown WS_2 MLs by encapsulating and sealing them with both top and bottom few-layer *h*-BN, as tested by subsequent high-temperature annealing up to 873 K and photoluminescence (PL) measurements. These transition-metal dichalcogenide (TMD) MLs remained stable up to this maximum temperature, as seen visually. After the heating/cooling cycle, the integrated photoluminescence (PL) intensity at 300 K in the $MoSe_2$ ML was ∼4 times larger than that before heating and that from exciton and trion PL in the analogous WS_2 ML sample was ∼14 times and ∼2.5 times larger at 77 K and the exciton peak was ∼9.5 times larger at 300 K. This is attributed to the reduction of impurities, the lateral expulsion of contamination leading to clean and atomically flat surfaces, and the sealing provided by the *h*-BN layers that prevents the diffusion of molecules such as trace O_2 and H_2O to the TMD ML. Stability and optical performance are much improved compared to that in earlier work using top *h*-BN only, in which the WS_2 ML PL intensity decreased even for an optimal gas environment. This complete encapsulation is particularly promising for CVD-grown TMD MLs because they have relatively more charge and other impurities than do exfoliated MLs. These results open a new route for improving the optical properties of TMD MLs and their performance and applications both at room and higher temperatures.

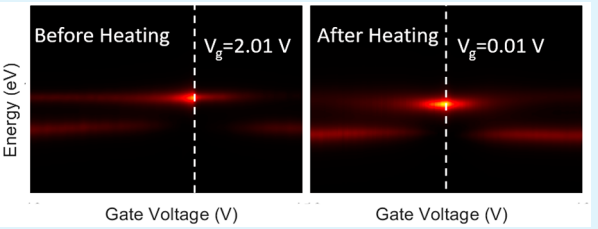

KEYWORDS: *$MoSe_2$ monolayers, WS_2 monolayers, h-BN encapsulation, exciton, trion, photoluminescence, high temperature processing*

INTRODUCTION

Two-dimensional transition-metal dichalcogenides (TMDs) have aroused intense attention, because of their exotic physical properties.[1−3] They can be useful for a wide range of applications in optical devices and optoelectronics,[4,5] such as photodetectors and light emitters.[6−8] All such applications require high optical quality of the TMDs with any disorder removed. There are several types of adsorbed species trapped between the individual layers during transfer in TMD stack fabrication. For graphene, high-temperature annealing has been proven to be effective in limiting extrinsic disorder and contamination from the external environment.[9−12] However, the major obstacles in advancing the use of TMDs includes their instability at high temperature. Bulk TMDs are known to be less stable at higher temperature, in oxygen-containing media, in inert gases, and under vacuum.[13,14]

Photoluminescence (PL) enhancement in TMD monolayers (MLs) has been reported in previous studies that has been attributed to chemical doping,[16−19] plasmonic effects,[20] and surface engineering.[21,22] For example, Nan et al. reported the PL enhancement of MoS_2 MLs by defect engineering and oxygen bonding at the defect sites.[22] In addition, Tyurnina et al. found that the PL intensity of TMDs can be enhanced by the funneling effect resulting from external strain.[23] In most of these studies, the PL increases are not from improving sample optical quality through the reduction of inhomogeneity and impurities, but by introducing defects at the surface and strain.

Improved properties by thermal annealing and better stability at elevated temperatures might be expected by encapsulating the TMD ML using hexagonal boron nitride (*h*-BN), which is known to be thermally stable at high temperature, before heating the TMD.[15] We have previously seen notable improvement in the stability and optical properties, notably PL, of chemical vapor deposition (CVD)-grown WS_2 monolayers (MLs) after heating/cooling cycles, relative to the bare ML, by first fully covering the WS_2 ML with multilayer *h*-BN.[24] However, although PL was stronger with a top layer of *h*-BN than without it, the intensity still decreased in these samples. Markedly better improvements in both properties and stability might be expected with the better sealing of the edges of the TMD monolayer expected from full

Received: October 1, 2021
Accepted: December 16, 2021
Published: December 31, 2021

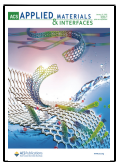

https://doi.org/10.1021/acsami.1c18991
ACS Appl. Mater. Interfaces 2022, 14, 2255−2262

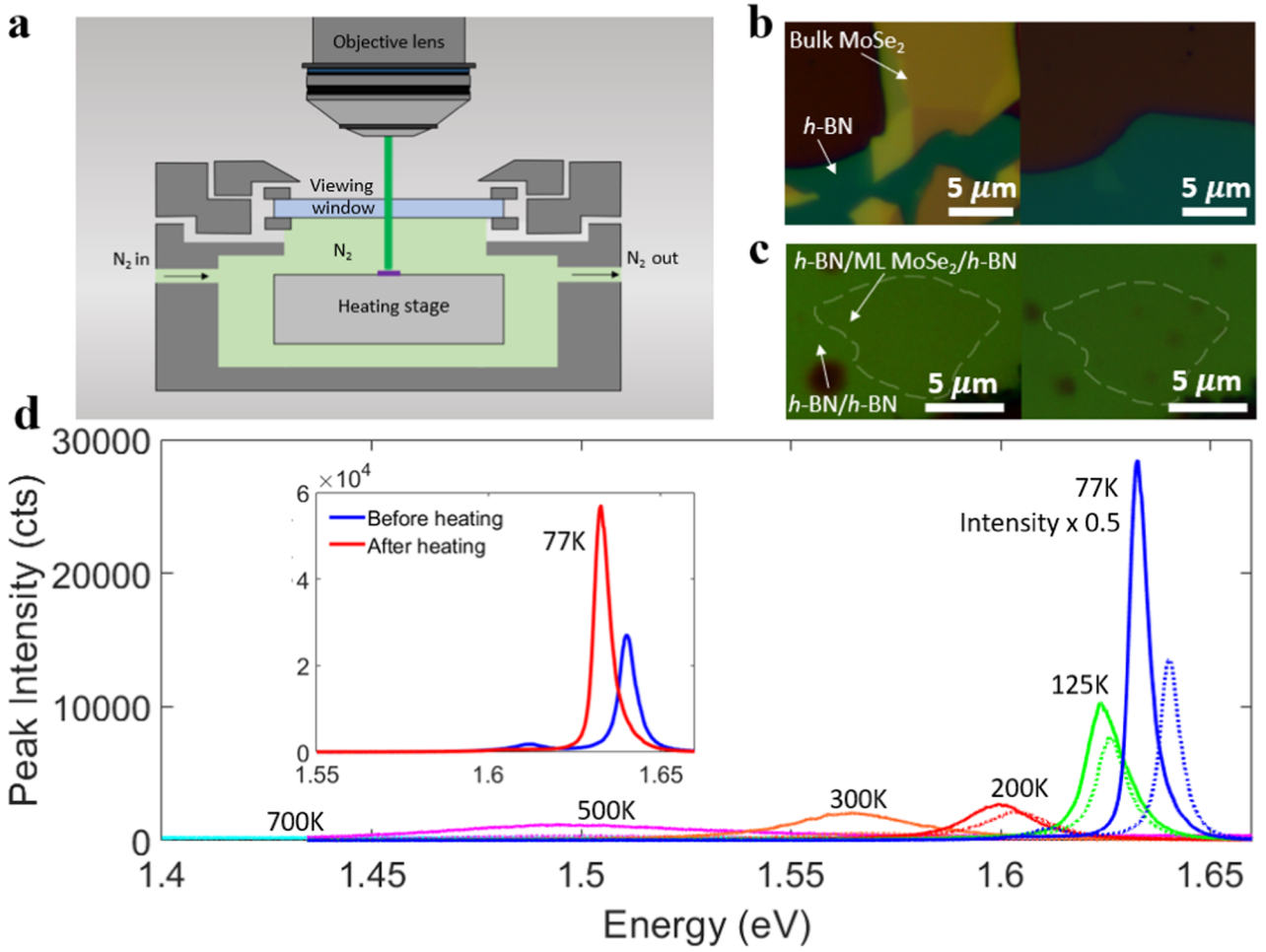

Figure 1. (a) Schematic of the *h*-BN/TMD ML/*h*-BN stack sample in a Linkam cell in which the temperature and gas environment are controlled. The argon-ion laser is focused by an Olympus long-working-distance (50×) objective, through the 22-mm-diameter and 0.5-mm-thick glass window. There is a liquid nitrogen cooling pump system and a temperature system controller with a platinum temperature sensor (not shown). (The water circulator system is not shown in the figure.) (b) The optical image at room temperature of bulk $MoSe_2$ on a SiO_2/Si substrate (without *h*-BN encapsulation) (left) before and (right) after heating to 873 K, showing the decomposition after heating. (c) The optical image at room temperature of the *h*-BN/$MoSe_2$/*h*-BN stack (left) before and (right) after heating to 873 K. (d) In situ PL of the $MoSe_2$ stack at selected temperatures during heating from 77 K to 873 K (dotted curves) and cooling from 873 K to 77 K (solid curves). Very weak PL was seen at 873 K (not shown), but the sample was intact. Half the intensity is plotted for both 77 K spectra (in blue). Inset shows PL spectra at 77 K (replotted).

encapsulation of the ML by using top and bottom *h*-BN with larger areas than the TMD, prepared by employing established transfer methods.[25] This would be expected to limit molecular diffusion between the TMD and the substrate.

We examine the impact of full encapsulation here, for two light-emitting TMD MLs. First, we investigate the exfoliated monolayer $MoSe_2$ in some detail and then, more briefly, the CVD-grown monolayer WS_2; the latter is investigated for a comparison with our previous work with top layer *h*-BN covering only. Moreover, because CVD-grown WS_2 MLs have more charge impurities, unintentional doping and other inhomogeneity and impurities (due the fabrication process) than do exfoliated WS_2 MLs,[26−28] any improvements seen here could be significantly more widespread, when the CVD-growth method is needed to fabricate the TMD ML.

$MoSe_2$ and WS_2 monolayers completely encapsulated by *h*-BN are seen to remain stable to 873 K here, with their PL being greatly increased after cycling to high temperature (873 K) with this encapsulation. In particular, this use of top and bottom *h*-BN layers greatly improved these properties of the CVD-grown WS_2 ML, both absolutely and relative to WS_2 with only top *h*-BN.

EXPERIMENTAL SECTION

An exfoliated $MoSe_2$ ML (with the largest lateral dimension being ∼5−10 μm) and several-layer *h*-BN (∼20−30 μm) flakes were exfoliated onto two different 285-nm SiO_2/Si substrates. (See Section S1 in the Supporting Information for details about exfoliation.) The $MoSe_2$ ML was characterized by optical microscopy, and the thickness and uniformity of the *h*-BN flakes were determined by atomic force microscopy (AFM) (20−40 nm). Stacks were prepared by using a dry transfer method with a polycaprolactone/polydimethylsiloxane slide (polycaprolactone (PCL), polydimethylsiloxane (PDMS)).[25] The top *h*-BN was picked up with PCL, and then this top *h*-BN was used to pick up the $MoSe_2$ ML and transfer it onto the bottom *h*-BN so that on the periphery of the $MoSe_2$ ML, the *h*-BN flakes, which were both much larger than the $MoSe_2$, were in contact. The samples were placed in a Linkam cell (LINKAM THMS 600), which enabled the in situ control of temperature and environment (see Figure 1a, as well as Figure S1 in the Supporting Information). λ = 514.5 nm CW laser light produced by an argon-ion laser illuminated the sample, in the presence of 25 sccm N_2 flowing during a heating/cooling cycle during which the temperature was increased from 77 K to 873 K and then

https://doi.org/10.1021/acsami.1c18991
ACS Appl. Mater. Interfaces 2022, 14, 2255−2262

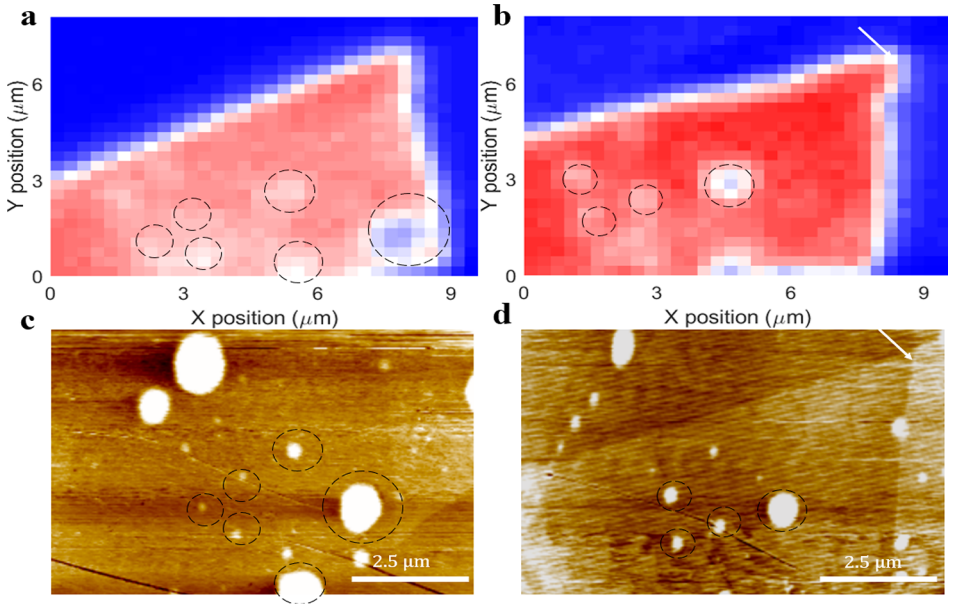

Figure 2. Spatially mapped peak PL intensity of the $MoSe_2$ ML sandwiched by *h*-BN at 300 K, taken (a) before and (b) after the heating/cooling cycle from 300 K to 873 K to 300 K. The AFM topography of this sample at 300 K is shown (c) before and (d) after this temperature cycling.

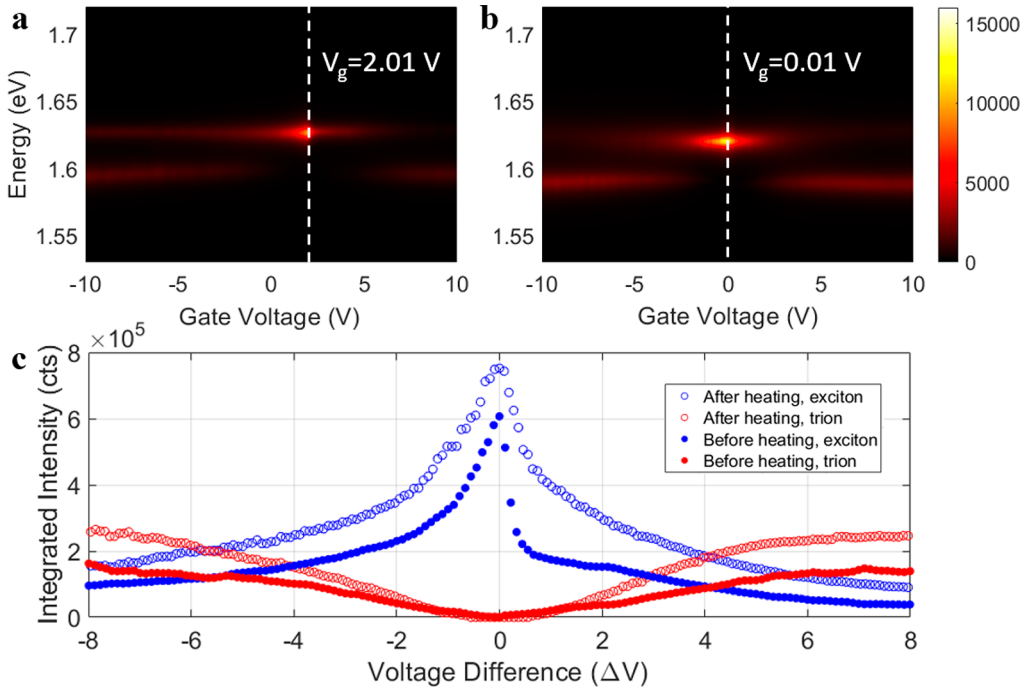

Figure 3. Gate-dependent photoluminescence of the $MoSe_2$ stack at 77 K plotted as PL intensity, with color indicating this intensity, versus the gate voltage (a) before the heating/cooling cycle (taken in ∼0.11 V steps) and (b) after this cycle (∼0.09 V steps). The dashed lines represent the charge neutrality points. There are two optical transition peaks at different gate voltage regions. The peak nearest 0 V is due to the exciton (X^0) and the lower-energy peak is either the negative trion (X^-) (at positive gate voltages) and the positive trion (X^+) (negative voltages). (c) The trion and exciton integrated intensities extracted from panels (a) and (b) versus the gate voltage difference from the charge neutrality point.

back down to 77 K. The focused laser was kept at specific set-points for ∼10 min during which *in situ* PL was captured by a cryogenically cooled silicon CCD detector array (Princeton Instruments, Model Spec-10:400B). (See Figure S2 in the Supporting Information for the optical setup.)

The left part of Figure 1c shows the optical image of an *h*-BN/$MoSe_2$/*h*-BN stack on the SiO_2/Si substrate at room temperature before temperature cycling. It also indicates the region outside the $MoSe_2$ ML where the top and bottom *h*-BN overlap. The left part of this figure gives the optical image of this same sample after the heating/cooling cycle. The area enclosed by the dashed line is the *h*-BN/$MoSe_2$/*h*-BN region. With complete encapsulation, optical imaging suggests the $MoSe_2$ ML is stable during this cycle. In contrast, without the *h*-BN encapsulation, even many-layer (bulk) $MoSe_2$ started to decompose above 773 K and the entire bulk $MoSe_2$ sample was no longer present at 873 K (Figure 1b, right side). In all optical comparisons, the optical images were taken at the same spot before and after the cycle. An *h*-BN flake was used as an alignment mark in Figure 1b. This shows that, with this complete encapsulation, $MoSe_2$ MLs are stable to higher temperatures than without it.

https://doi.org/10.1021/acsami.1c18991
ACS Appl. Mater. Interfaces 2022, 14, 2255−2262

Figure 1d shows the PL spectra of monolayer $MoSe_2$ in this *h*-BN/$MoSe_2$/*h*-BN stack during the heating and cooling cycles, taken while the sample was at the indicated temperature for 10 min. PL at selected temperatures is shown. Data from all PL measurements are given in Figure S3 in the Supporting Information. The PL spectra generally follow similar trends at corresponding temperatures within the heating and cooling cycles, but the peak PL intensities are larger during the cooling cycle, as detailed below and in Figure S3.

Then we spatially mapped the peak PL intensity across a second monolayer $MoSe_2$ sandwich stack (Figure 2), which was prepared in the same way as the one used for Figures 1b and 1c, in the ambient environment by using a 532-nm CW laser (frequency-doubled Nd^{3+}:YAG) for excitation. After mapping this stack at ambient temperature (Figure 2a), it was placed in the Linkam cell for a 300 to 873 K to 300 K heating/cooling cycle, and then it was mapped again (Figure 2b). The maps have three distinctive features. First, the PL intensity after heating is greater than before heating, as noted previously. Second, both the line shapes and integrated area profiles of the PL patterns are largely unchanged after heating, indicating that the $MoSe_2$ flake does not decompose or become damaged during heating and that it is well-protected by the complete *h*-BN encapsulation. Third, the PL intensity changes from before heating to after heating are uniformly distributed across the entire sample, which means the PL changes are not due to localized defects generated by O_2 or other molecules penetrating beneath the overlayer, as in ref 22. (See Figures 2a and 2b.)

Figure 2c presents the AFM trace of this same $MoSe_2$ stack before the heating/cooling cycle. There are several large bubbles on the $MoSe_2$ flake that likely correspond to adsorbents and contamination formed during the transfer process. Figure 2d is the AFM image of the same sample taken after the heating cycle. Figure 2d shows that, after heating, there are fewer bubbles and they are larger, suggesting that they have coalesced, and they are now at the lateral edges of the $MoSe_2$ flake and seem to have migrated there. The locations of the bubbles match the respective lower PL intensity regions in Figures 2a and 2b. In particular, there is a large bubble on the bottom right of the sample in Figure 2c that corresponds to the large low-PL-intensity area in Figure 2a. Moreover, the boundaries of the $MoSe_2$ ML in the encapsulated *h*-BN/$MoSe_2$/*h*-BN stack are clearer and sharper in the AFM images after heating (Figure 2d), which indicates that the vertical separations between the $MoSe_2$ and the *h*-BN layers have decreased (Figures 2c and 2d).

Electrical gating is an effective way to control the carrier concentration level in ML TMDs.[29,30] To this end, we first performed gate-dependent PL measurements (514.5 nm) with an *h*-BN/$MoSe_2$/*h*-BN field effect transistor at 77 K under vacuum (~10^{-6} Torr) with gate voltage biasing using a Keithley Model 2400 source meter. Then a stack, prepared as were the two samples used in Figures 1 and 2, underwent a heating/cooling cycle in a separate oven (300 K to 873 K to 300 K), with a flow of 25 sccm N_2 gas. Gate-dependent PL was then re-examined at 77 K. Figure 3a presents a color map of the PL intensity of this stack of completely encapsulated $MoSe_2$ at a fixed pump laser power (~0.3 mW, with ~1 μm spot size), as a function of gate voltage from −10 V to 10 V, before the heating/cooling cycle. There are two optical transition peaks at each gate voltage. The PL peak nearest 0 V is due to excitons (X^0). The second, lower energy emission peak at large magnitude gate biases corresponds to either the negative trion (X^-) (for positive voltage) or the positive trion (X^+) (negative voltage). Figure 3b presents a color map of the PL intensity, as a function of gate voltage over the same voltage range for this same sample after the heating/cooling cycle. Figure 3c plots the integrated PL intensities of the exciton and trion peaks before and after the heating cycle.

Completely encapsulated *h*-BN/CVD-grown WS_2/*h*-BN stacks were fabricated by first growing WS_2 ML triangles (~5 μm largest lateral dimension) by CVD on one 285 nm SiO_2/Si substrate, as in ref 31. Then, *h*-BN flakes were exfoliated on a second 285-nm SiO_2/Si substrate; AFM was used to determine their thickness and uniformity (with lateral dimension and thickness as before). Stacks were then prepared by spin coating a poly(propylene) carbonate (PPC) layer and then two cellulose acetate butyrate (CAB) layers on the substrate with the WS_2 flakes.[32] The SiO_2 layer on the Si was etched with potassium hydroxide (KOH) solution, leaving the PPC/CAB layers with several WS_2 ML flakes at the surface of this solution. One WS_2 ML flake (with the PPC/CAB) was transferred onto the *h*-BN flake serving as the bottom *h*-BN by using a glass slide with PDMS and PPC, and then the CAB layer was removed with the slide. The *h*-BN flake serving as the top *h*-BN layer was picked up with a PPC/PDMS glass slide and transferred onto the WS_2/bottom *h*-BN assembly to form the completely encapsulated WS_2 stack.

Figure 4 shows the PL spectra of this WS_2 stack at 77 K before (blue) and after (red) the 77 K to 873 K to 77 K heating/cooling cycle. The two optical transition peaks in each spectrum again correspond to the exciton peak at higher energy and the trion peaks at lower energy.

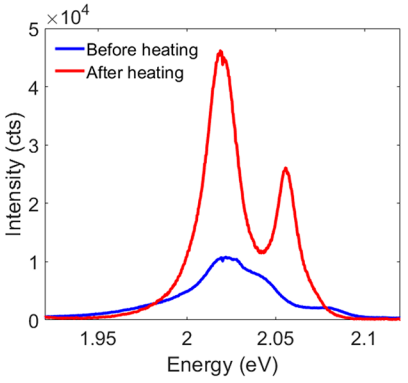

Figure 4. PL spectra of the CVD-grown ML WS_2 sandwiched by several-layer top and bottom *h*-BN, at 77 K (514.5 nm excitation), before and after the heating/cooling cycle.

RESULTS AND DISCUSSION

Both TMD ML stacks seem to be structurally stable during the heating cycle, with no changes in material structure. The WS_2 ML stack appears to be stable because the Raman spectrum is the same before and after (see Figure S4 in the Supporting Information). Because the stability of this CVD-grown ML is thought to be worse than that for a corresponding exfoliated ML,[26−28] the $MoSe_2$ ML stack is also expected to be stable, as is confirmed by the optical microscopy image of the first $MoSe_2$ ML stack in Figure 1c, and the AFM images of the second stack before heating (Figure 2c) and after heating (Figure 2d). The heating cycle narrows the PL widths (inset to Figure 1d), further confirming the stability of this stack. Also, the decrease in the PL widths suggests fewer defects and that there are no new PL peaks after annealing, suggests that there are no new defects.

As seen in Figure 1d, the integrated $MoSe_2$ PL intensity at 300 K from the stack after the heating/cooling cycle is ~4 times that before it. Both have PL peaks located at ~1.57 eV, but there is a small red shift of 4 meV after the cycle, which is likely due to a reduction in strain during the heating process.[33−35] This corresponds to an increase in the biaxial in-plane tensile strain of ~0.12% if all of it were due to strain.[36] Because $MoSe_2$ MLs have a larger thermal expansion coefficient than does Si but is similar to that of *h*-BN,[37−39] an increase in this strain during the cooling cycle is expected with adhesion between $MoSe_2$ and the substrate (an increase of ~0.26%).

The peak width is 40.5 meV (fwhm) before the cycle and 36.1 meV after it. This narrowing could mean that the exciton

https://doi.org/10.1021/acsami.1c18991
ACS Appl. Mater. Interfaces 2022, 14, 2255−2262

lifetime is longer after the cycle, there are fewer impurities, and/or there is a reduction in inhomogeneity (some of which may have been introduced during sample preparation).[26−28] At room temperature, the decay time is usually not only dominated by radiative recombination processes but rather by nonradiative recombination processes.

The inset in Figure 1d shows the PL spectra at 77 K of the same $MoSe_2$ stack at the start (blue) and end (red) of the heating/cooling cycle. There are two peaks in each spectrum, corresponding to the exciton peaks (the larger, higher-energy peaks) and trion peaks (the smaller, lower-energy peaks). (The trion peak is very small at the end of the cycle.) As observed at 300 K, at 77 K, the integrated PL intensity is larger after the cycle (now ∼4 times that before it). The exciton emission energy after the heating/cooling cycle has a slight red shift (7 meV) at 77 K, compared to the peak position before the cycle, again which is likely due to a reduction in strain during heating.[33−35] This corresponds to an increase in the biaxial in-plane tensile strain of ∼0.21% if it were all due to strain,[36] as noted above. Also, the peak widths of the exciton peaks are ∼5 meV, and they are slightly smaller after the cycle, by ∼0.4 meV.

As noted above, Figure 2 suggests that adsorbents and contamination formed during the transfer process diffuse and aggregate into bubbles. During heating, these bubbles are laterally expelled from the interfaces between the TMD and the upper and lower *h*-BN, and coalesce into larger bubbles, and this leaves much of these interfaces clean and atomically flat. This adsorbent and contamination diffusion can contribute to PL enhancement and the reduction of inhomogeneity could contribute to the PL line shape narrowing. At the same time, the $MoSe_2$ flakes are well-protected by the *h*-BN encapsulation layer during the high-temperature annealing.

In Figure 3a, before the heating/cooling cycle, the charge-neutrality point (with the maximum exciton density and with equal electron and hole densities) is highlighted by the dashed line at ∼2.01 V. This means that, initially, it is *p*-type. With more positive gate voltage, there are additional free electrons added in the sample and the exciton (X^0) population decreases and negative trions (X^-) are more likely to be formed, and the material shows more *n*-type doping. In contrast, when a negative voltage is applied, additional holes are added and it becomes more *p*-type, and now the X^0 peak decreases as the positive trion X^+ peak appears, more so at larger negative voltages.[40] From the peak separation of exciton and trion, the trion binding energy is ∼33 meV. For the same (magnitude of the) gate voltage, relative to its respective offset, the X^+ peaks are shifted from the X^0 peak by ∼1−3 meV more than the corresponding X^- peaks, mainly due to Coulomb interactions, as has been observed in other work.[29]

In Figure 3b, the trion binding energy after the heating/cooling cycle is the same as that before it (Figure 3a). Also, all peaks undergo an ∼10 meV red shift due to this cycle, which is likely due to a reduction in strain during the heating.[33−35] This corresponds to an increase in the biaxial in-plane tensile strain of ∼0.3% if it were all due to strain,[36] as noted above.

After the heating/cooling cycle the charge-neutrality point of the $MoSe_2$ ML PL is at the dashed line, ∼0.01 V, in Figure 3b, which is shifted by approximately −2 V, compared to that in Figure 3a before the cycle. This shows that the intrinsic carrier concentration has changed. The $MoSe_2$ ML became less *p*-type doped, with the hole carrier density changing by $\Delta n \approx -1.1 \times 10^{12}$ cm^{-2} (see Section S5 in the Supporting Information). This intrinsic carrier concentration change leads to the observed PL enhancement, because of the passivation of nonradiative recombination centers in the sample.[40] In addition to charge impurities, two other possible disorder sources could contribute to *p*-type doping in the sample before heating. One is the contamination trapped between the $MoSe_2$/*h*-BN interfaces during the stacking process. The contamination trapped at these interfaces is mostly due to hydrocarbon molecules, causing the *p*-type dopants that shift the charge neutrality gate voltage to positive voltages.[41] The other sources of contamination are the residual O_2 and H_2O molecules trapped at these interfaces, which also introduce *p*-type doping.[22] Our work shows that bubbles, presumably of these molecules, are formed and move during heating to the periphery, leading to atomically flat and clean graphene and *h*-BN interfaces, as others have also seen,[10−12] and, moreover, we see that this leads to enhanced PL. Adsorbents and contamination formed during the transfer diffuse and are laterally expelled from the interfaces, so these interfaces are mostly clean and atomically flat. Unintentionally trapped charges are also removed, which results in switching the dominant PL from excitons and trions to mostly that from excitons, as has also been done by others by using chemical doping.[42]

After first extracting the gate-voltage-dependent exciton and trion peaks from both Figures 3a and 3b, in Figure 3c, we plot the integrated exciton and trion intensities vs gate voltage shifted so the charge-neutrality points of each is 0 V. This enables comparison of the PL intensities at the same doping density. These plots clearly show that the integrated $MoSe_2$ PL from the stack after the heating/cooling cycle is larger for both excitons and trions than before it. This PL intensity increase is expected to be due to not only the doping level reduction see here.[42] Because these data specifically compare PL intensities at a fixed doping density (Figure 3c), they indicate the suppression of nonradiative decay due to the reduction of the impurities that arise from ML preparation and handling. These latter impurities are being removed, as seen in the formation of clean and atomic flat interfaces in Figures 2c and 2d, and this also increases the PL.

Complete *h*-BN encapsulation and annealing might improve the stability and optical properties of other TMD MLs as well by also reducing doping levels via removing unintentionally trapped charges at the interfaces and by making them atomically flat and clear (Figure 2). In particular, it may be very promising to do this for CVD-grown ML samples, because they usually have even more unintentional doping than do samples exfoliated from crystals,[26−28] as well as other impurities and defects from sample fabrication and preparation,[41] and so CVD-grown TMD MLs are less stable than corresponding exfoliated samples. The degradation and decomposition of TMDs result from oxygen dissociating into individual atoms and adsorbing on the surfaces of the TMD flakes. The TMD can be stable at room temperature and even at elevated temperatures because decomposition is limited by the large energy barrier for O_2 dissociation and chemisorption.[43] However, defects can dramatically lower this barrier and make decomposition possible at lower temperatures, and even at room temperature.[43,44]

Figure 4 shows the PL spectra of the completely encapsulated WS_2 stack at 77 K before (blue) and after (red) the 77 K to 873 K to 77 K heating/cooling cycle. The two main optical transition peaks in each spectrum again correspond to the exciton peak at higher energy and the trion

https://doi.org/10.1021/acsami.1c18991
ACS Appl. Mater. Interfaces 2022, 14, 2255−2262

peak at lower energy. Whereas the exciton and trion PL peaks for the $MoSe_2$ stack are fit well with a Lorentzian line shape, those peaks in CVD-grown WS_2 are well fit this way only after heating. Those before heating are severely and asymmetrically broadened by inhomogeneities, so these two peaks were fit with a Gaussian distribution.

The exciton and trion peak widths at 77 K are 14.2 and 56.4 meV (fwhm), respectively, before the heating/cooling cycle, and 12.6 and 20.7 meV after it. The peak PL intensity was larger after the annealing cycle than that before it, by ∼14 times for the exciton and ∼2.5 times for the trion. (The dark exciton effect lowers the overall PL intensity.[45−47]) After the heating cycle, the peaks are red-shifted relative to those before, by 4.6 meV for the trion peak and 26.9 meV for the exciton.[33−35] These exciton peak red shifts correspond to an increase in the biaxial in-plane tensile strain of ∼0.04%−0.26% if it were all due to strain,[24,48] as noted above. Also, the trion peak red shift of ∼22 meV is more indicative of the reduction of trion binding energy. As is shown in Figure 2d, after heating, the decreasing of vertical separations in van der Waals heterostructures between the $MoSe_2$ and the *h*-BN layers results in changes in the surrounding dielectric environment. This change can heavily reduce the trion binding energy. By the calculation from Florian et al., a 5 Å interlayer gap between *h*-BN-$MoSe_2$-*h*-BN can cause a trion binding energy difference of ∼15−20 meV.[49]

In our earlier paper,[24] a CVD-grown WS_2 ML was seen to be more stable and had larger integrated PL at 300 K after a 300 K to 873 K to 300 K heating/cooling cycle with a top *h*-BN layer than without it and with nitrogen flow, rather than in ambient air or with flowing forming gas. However, the PL was still smaller than before the cycle, by ∼47%. Therefore, the top *h*-BN level helped the stability somewhat, but improvement was still needed. As seen in Figure 4, now with complete encapsulation, after a 77 K to 873 K to 77 K cycle, the WS_2 ML PL peak and integrated intensities no longer decrease but increase. Measured at 300 K, during cooling rampdown, it is ∼9.5 times larger than that before the heating rampup, with purging N_2.

One reason for this marked improvement with full encapsulation is that with top-layer *h*-BN and no bottom-layer *h*-BN, trace residual molecules such as O_2 and H_2O, present with nitrogen flow, still diffuse between the WS_2 ML and the SiO_2 substrate, because of its roughness and dangling bonds; this leads to some degradation in PL during heating, although the sample does not decompose. This diffusion does not occur with complete encapsulation and sealing of the *h*-BN sandwich. Other reasons for this improvement are noted above. Because the PL intensity exhibits a dramatic enhancement for this CVD-grown ML with complete encapsulation, this technique is expected to be especially useful for other CVD-grown samples as well, whose performance is also hurt by the known higher levels of impurities introduced by CVD.

The increases in PL intensities for both ML stacks that result from the heating cycle are thought to be due to decreased impurities, as detailed above. One other potential factor could be the changes in strain of the TMD MLs. Lloyd et al. measured the integrated PL intensity change of ML MoS_2, as a function of biaxial in-plane tensile strain,[50] and using this as a guide for both TMD MLs studied here, there is an estimated increase in biaxial in-plane tensile strain of ∼0.21% for the $MoSe_2$ ML and ∼0.26% for the WS_2 ML; this corresponds to a decrease in PL integrated intensity of ∼20% for the $MoSe_2$ ML and ∼25% for the WS_2 ML. However, we observed that PL was stronger by a factor of 4 for the $MoSe_2$ stack and by a factor of 9.5 for the WS_2 stack. The observed PL shifts are consistent with strain changes due to thermal expansion, but the increases in the PL intensities do not appear to originate from the changes in strain.

Another possible cause for the PL increases is dielectric screening effects due to the changes in bubbles in the heating cycle, as seen above in the $MoSe_2$ stack in Figure 2. Fu et al. showed that dielectric screening by *h*-BN leads to a peak PL intensity increase of ∼60% (in that case, for a WS_2 ML), which corresponds to a much smaller integrated PL intensity increase than this, and which was not given, because the PL width was then much smaller.[51] The increase in integrated PL from the bubble regions would be expected to be locally weaker due to less optical dielectric screening, and this is seen. The integrated PL intensity is weaker from the three bubbles seen in Figure 2a than that from the flat regions by ∼16%, 21%, and 38% for the bubbles with diameters of ∼0.3, 0.14, and 1.1 μm, respectively. Therefore, the motion and changes in the bubbles due to heating do not cause the increases seen in the PL intensity.

CONCLUSIONS

Sealing $MoSe_2$ and WS_2 MLs with top and bottom *h*-BN encapsulation flakes improves their thermal stability at high temperature, as tested in a heating/cooling cycle, and increases their PL. The increased PL likely occurs because impurities are laterally expelled from the TMD stack during heating (and so the TMD ML interfaces also become flatter). The increased PL also occurs, along with material stability, because other impurities, such as of trace residual molecules such as O_2 and H_2O present with, for example, nitrogen flow, cannot enter during heating since the TMD MLs are sealed at the edges. The reduction of impurities is particularly important for CVD-grown ML samples, such as for the WS_2 ML here. Encapsulation by only top *h*-BN is not sufficient to achieve these improvements. These improvements are generally expected for TMD MLs, and these methods can be used in applications.

ASSOCIATED CONTENT

Supporting Information

The Supporting Information is available free of charge via the Internet at . The Supporting Information is available free of charge at https://pubs.acs.org/doi/10.1021/acsami.1c18991.

More details concerning monolayer exfoliation; schematic view of the Linkham THMS 600; the experimental setup; temperature dependence of photoluminescence; carrier concentration calculation; and room-temperature Raman analysis of monolayer WS_2 before and after heating (PDF)

AUTHOR INFORMATION

Corresponding Authors

Irving P. Herman − *Department of Applied Physics and Applied Mathematics, Columbia University, New York, New York 10027, United States;* orcid.org/0000-0001-8492-6000; Email: iph1@columbia.edu

Bumho Kim − *Department of Mechanical Engineering, Columbia University, New York, New York 10027, United States; Department of Physics and Astronomy, University of Pennsylvania, Philadelphia, Pennsylvania 19104, United*

https://doi.org/10.1021/acsami.1c18991
ACS Appl. Mater. Interfaces 2022, 14, 2255−2262

States; Present Address: Currently with the Department of Physics and Astronomy, University of Pennsylvania, Lehigh, PA, USA (B. Kim).; orcid.org/0000-0002-5671-5641; Email: bk2600@columbia.edu

Authors

Xiang Hua − *Department of Applied Physics and Applied Mathematics, Columbia University, New York, New York 10027, United States;* orcid.org/0000-0001-8834-5932

Theodor Axenie − *Department of Applied Physics and Applied Mathematics, Columbia University, New York, New York 10027, United States*

Mateo Navarro Goldaraz − *Department of Applied Physics and Applied Mathematics, Columbia University, New York, New York 10027, United States*

Kyungnam Kang − *Department of Mechanical Engineering, Stevens Institute of Technology, Hoboken, New Jersey 07030, United States*

Eui-Hyeok Yang − *Department of Mechanical Engineering, Stevens Institute of Technology, Hoboken, New Jersey 07030, United States;* orcid.org/0000-0003-4893-1691

Kenji Watanabe − *Research Center for Functional Materials, National Institute for Materials Science, Tsukuba 305-0044, Japan;* Present Address: Currently with the Research Center for Functional Materials, National Institute for Materials Science, 1−1 Namiki, Tsukuba, 305-0044, Japan (K. Watanabe); orcid.org/0000-0003-3701-8119

Takashi Taniguchi − *International Center for Materials Nanoarchitectonics, National Institute for Materials Science, Tsukuba 305-0044, Japan;* Present Address: Currently with International Center for Materials Nanoarchitectonics, National Institute for Materials Science, 1−1 Namiki, Tsukuba, 305-0044, Japan (T. Taniguchi).; orcid.org/0000-0002-1467-3105

James Hone − *Department of Mechanical Engineering, Columbia University, New York, New York 10027, United States*

Complete contact information is available at: https://pubs.acs.org/10.1021/acsami.1c18991

Author Contributions

The paper was written through contributions of all authors. All authors have given approval to the final version of the paper.

Funding

This work was supported by the IGERT program of the National Science Foundation (No. DGE-1069240).

Notes

The authors declare no competing financial interest.

■ ACKNOWLEDGMENTS

This work was supported by the IGERT program of the National Science Foundation (DGE-1069240). K.W. and T.T. acknowledge support from the Elemental Strategy Initiative conducted by the MEXT, Japan (Grant No. JPMXP0112101001) and JSPS KAKENHI (Grant Nos. 19H05790, 20H00354, and 21H05233).

■ REFERENCES

(1) Wang, Q. H.; Kalantar-Zadeh, K.; Kis, A.; Coleman, J. N.; Strano, M. S. Electronics and optoelectronics of two-dimensional transition metal dichalcogenides. *Nat. Nanotechnol.* **2012**, *7*, 699−712.

(2) Mak, K. F.; Lee, C.; Hone, J.; Shan, J.; Heinz, T. F. Atomically Thin MoS_2: A New Direct-Gap Semiconductor. *Phys. Rev. Lett.* **2010**, *105*, 136805.

(3) Splendiani, A.; Sun, L.; Zhang, Y.; Li, T.; Kim, J.; Chim, C.-Y.; Galli, G.; Wang, F. Emerging Photoluminescence in Monolayer MoS_2. *Nano Lett.* **2010**, *10*, 1271−1275.

(4) Wu, S.; Buckley, S.; Schaibley, J. R.; Feng, L.; Yan, J.; Mandrus, D. G.; Hatami, F.; Yao, W.; Vučković, J.; Majumdar, A.; Xu, X. Monolayer semiconductor nanocavity lasers with ultralow thresholds. *Nature* **2015**, *520*, 69−72.

(5) Palacios-Berraquero, C.; Barbone, M.; Kara, D. M.; Chen, X.; Goykhman, I.; Yoon, D.; Ott, A. K.; Beitner, J.; Watanabe, K.; Taniguchi, T.; Ferrari, A. C.; Atatüre, M. Atomically thin quantum light-emitting diodes. *Nat. Commun.* **2016**, *7*, 12978.

(6) Yin, Z.; Li, H.; Li, H.; Jiang, L.; Shi, Y.; Sun, Y.; Lu, G.; Zhang, Q.; Chen, X.; Zhang, H. Single-Layer MoS_2 Phototransistors. *ACS Nano* **2012**, *6*, 74−80.

(7) Lopez-Sanchez, O.; Lembke, D.; Kayci, M.; Radenovic, A.; Kis, A. Ultrasensitive Photodetectors based on Monolayer MoS_2. *Nat. Nanotechnol.* **2013**, *8*, 497−501.

(8) Baugher, B. W.; Churchill, H. O.; Yang, Y.; Jarillo-Herrero, P. Optoelectronic Devices based on Electrically Tunable pn Diodes in a Monolayer Dichalcogenide. *Nat. Nanotechnol.* **2014**, *9*, 262−267.

(9) Lin, Y.-C.; Lu, C.-C.; Yeh, C.-H.; Jin, C.; Suenaga, K.; Chiu, P.-W. Graphene Annealing: How Clean Can It Be? *Nano Lett.* **2012**, *12*, 414−419.

(10) Xie, W.; Weng, L.-T.; Ng, K. M.; Chan, C. K.; Chan, C.-M. Clean graphene surface through high temperature annealing. *Carbon.* **2015**, *94*, 740−748.

(11) Haigh, S. J.; Gholinia, A.; Jalil, R.; Romani, S.; Britnell, L.; Elias, D. C.; Novoselov, K. S.; Ponomarenko, L. A.; Geim, A. K.; Gorbachev, R. Cross-sectional imaging of individual layers and buried interfaces of graphene-based heterostructures and superlattices. *Nat. Mater.* **2012**, *11*, 764−767.

(12) Woods, C. R.; Withers, F.; Zhu, M. J.; Cao, Y.; Yu, G.; Kozikov, A.; Ben Shalom, M.; Morozov, S. V.; van Wijk, M. M.; Fasolino, A.; Katsnelson, M. I.; Watanabe, K.; Taniguchi, T.; Geim, A. K.; Mishchenko, A.; Novoselov, K. S. Macroscopic self-reorientation of interacting two-dimensional crystals. *Nat. Commun.* **2016**, *7*, 10800.

(13) Ross, S.; Sussman, A. Surface Oxidation of Molybdenum Disulfide. *J. Phys. Chem.* **1955**, *59*, 889−892.

(14) Cannon, P. Melting Point and Sublimation of Molybdenum Disulphide. *Nature* **1959**, *183*, 1612−1613.

(15) Liu, Z.; Gong, Y.; Zhou, W.; Ma, L.; Yu, J.; Idrobo, J. C.; Jung, J.; MacDonald, A. H.; Vajtai, R.; Lou, J.; Ajayan, P. M. Ultrathin high-temperature oxidation-resistant coatings of hexagonal boron nitride,. *Nature Commun.* **2013**, *4*, 2541.

(16) Tongay, S.; Zhou, J.; Ataca, C.; Liu, J.; Kang, J. S.; Matthews, T. S.; You, L.; Li, J. B.; Grossman, J. C.; Wu, J. Broad-Range Modulation of Light Emission in Two-Dimensional Semiconductors by Molecular Physisorption Gating. *Nano Lett.* **2013**, *13*, 2831−2836.

(17) Mouri, S.; Miyauchi, Y.; Matsuda, K. Tunable Photoluminescence of Monolayer MoS_2 via Chemical Doping. *Nano Lett.* **2013**, *13*, 5944−5948.

(18) Atallah, T. L.; Wang, J.; Bosch, M.; Seo, D.; Burke, R. A.; Moneer, O.; Zhu, J.; Theibault, M.; Brus, L. E.; Hone, J.; Zhu, X. Y. Electrostatic Screening of Charged Defects in Monolayer MoS_2. *J. Phys. Chem. Lett.* **2017**, *8*, 2148−2152.

(19) Hu, P.; Ye, J.; He, X.; Du, K.; Zhang, K. K.; Wang, X.; Xiong, Q.; Liu, Z.; Jiang, H.; Kloc, C. Control of Radiative Exciton Recombination by Charge Transfer Induced Surface Dipoles in MoS_2 and WS_2 Monolayers. *Sci. Rep* **2016**, *6*, 24105.

(20) Choi, S. Y.; Yip, C. T.; Li, G.-C.; Lei, D. Y.; Fung, K. H.; Yu, S. F.; Hao, J. Photoluminescence enhancement in few-layer WS_2 films via Au nanoparticles. *AIP Adv.* **2015**, *5*, 067148.

(21) Park, J. H.; Sanne, A.; Guo, Y.; Amani, M.; Zhang, K.; Movva, H. C. P.; Robinson, J. A.; Javey, A.; Robertson, J.; Banerjee, S. K.; Kummel, A. C. Defect passivation of transition metal dichalcogenides

via a charge transfer van der Waals interface. *Sci. Adv.* **2017**, *3*, No. e1701661.
(22) Nan, H.; Wang, Z.; Wang, W.; Liang, Z.; Lu, Y.; Chen, Q.; He, D.; Tan, P.; Miao, F.; Wang, X.; Wang, J.; Ni, Z. Strong Photoluminescence Enhancement of MoS_2 through Defect Engineering and Oxygen Bonding. *ACS Nano* **2014**, *8*, 5738−5745.
(23) Tyurnina, A. V.; Bandurin, D. A.; Khestanova, E.; Kravets, V. G.; Koperski, M.; Guinea, F.; Grigorenko, A. N.; Geim, A. K.; Grigorieva, I. V. Strained Bubbles in van der Waals Heterostructures as Local Emitters of Photoluminescence with Adjustable Wavelength. *ACS Photonics* **2019**, *6*, 516−524.
(24) Hua, X.; Zhang, D.; Kim, B.; Seo, D.; Kang, K.; Yang, E.-H.; Hu, J.; Chen, X.; Liang, H.; Watanabe, K.; Taniguchi, T.; Hone, J.; Kim, Y. D.; Herman, I. P. Stabilization of Chemical-Vapor-Deposition-Grown WS_2 Monolayers at Elevated Temperature with Hexagonal Boron Nitride Encapsulation. *ACS Appl. Mater. Interfaces* **2021**, *13*, 31271−31278.
(25) Wang, L.; Meric, I.; Huang, P. Y.; Gao, Q.; Gao, Y.; Tran, H.; Taniguchi, T.; Watanabe, K.; Campos, L. M.; Muller, D. A.; Guo, J.; Kim, P.; Hone, J.; Shepard, K. L.; Dean, C. R. One-Dimensional Electrical Contact to a Two-Dimensional Material. *Science* **2013**, *342*, 614.
(26) Hong, J.; Hu, Z.; Probert, M.; Li, K.; Lv, D.; Yang, X.; Gu, L.; Mao, N.; Feng, Q.; Xie, L.; Zhang, J.; Wu, D.; Zhang, Z.; Jin, C.; Ji, W.; Zhang, X.; Yuan, J.; Zhang, Z. Exploring Atomic Defects in Molybdenum Disulphide Monolayers. *Nat. Commun.* **2015**, *6*, 6293.
(27) Liu, Z.; Suenaga, K.; Wang, Z.; Shi, Z.; Okunishi, E.; Iijima, S. Identification of Active Atomic Defects in a Monolayered Tungsten Disulphide Nanoribbon. *Nat. Commun.* **2011**, *2*, 213.
(28) Gao, Y.; Liu, Z.; Sun, D.-M.; Huang, L.; Ma, L.-P.; Yin, L.-C.; Ma, T.; Zhang, Z.; Ma, X.-L.; Peng, L.-M.; Cheng, H.-M.; Ren, W. Large-Area Synthesis of High-Quality and Uniform Monolayer WS_2 on Reusable Au Foils. *Nat. Commun.* **2015**, *6*, 8569.
(29) Shepard, G. D.; Ardelean, J. V.; Ajayi, O. A.; Rhodes, D.; Zhu, X.; Hone, J. C.; Strauf, S. Trion-Species-Resolved Quantum Beats in $MoSe_2$. *ACS Nano* **2017**, *11*, 11550−11558.
(30) Ross, J. S.; Wu, S.; Yu, H.; Ghimire, N. J.; Jones, A. M.; Aivazian, G.; Yan, J.; Mandrus, D. G.; Xiao, D.; Yao, W.; Xu, X. Electrical Control of Neutral and Charged Excitons in a Monolayer Semiconductor. *Nat. Commun.* **2013**, *4*, 1474.
(31) Kang, K. N.; Godin, K.; Yang, E.-H. The Growth Scale and Kinetics of WS_2 Monolayers Under Varying H_2 Concentration. *Sci. Rep.* **2015**, *5*, 13205.
(32) Schneider, G. F.; Calado, V. E.; Zandbergen, H.; Vandersypen, L. M. K.; Dekker, C. Wedging Transfer of Nanostructures. *Nano Lett.* **2010**, *10*, 1912−1916.
(33) Zhu, C. R.; Wang, G.; Liu, B. L.; Marie, X.; Qiao, X. F.; Zhang, X.; Wu, X. X.; Fan, H.; Tan, P. H.; Amand, T.; Urbaszek, B. Strain tuning of optical emission energy and polarization in monolayer and bilayer MoS_2. *Phys. Rev. B* **2013**, *88*, 121301.
(34) Shi, H.; Pan, H.; Zhang, Y.-W.; Yakobson, B. I. Quasiparticle Band Structures and Optical Properties of Strained Monolayer MoS_2 and WS_2. *Phys. Rev. B* **2013**, *87*, 155304.
(35) Island, J. O.; Kuc, A.; Diependaal, E. H.; Bratschitsch, R.; van der Zant, H. S. J.; Heine, T.; Castellanos-Gomez, A. Precise and Reversible Band Gap Tuning in Single-Layer $MoSe_2$ by Uniaxial Strain. *Nanoscale* **2016**, *8*, 2589−2593.
(36) Frisenda, R.; Drüppel, M.; Schmidt, R.; Michaelis de Vasconcellos, S.; Perez de Lara, D.; Bratschitsch, R.; Rohlfing, M.; Castellanos-Gomez, A. Biaxial Strain Tuning of the Optical Properties of Single-Layer Transition Metal Dichalcogenides. *npj 2D Mater. Appl.* **2017**, *1*, 10.
(37) El-Mahalawy, S. H.; Evans, B. L. The Thermal Expansion of 2H-MoS_2, 2H-$MoSe_2$ and 2H-WSe_2 between 20 and 800°C. *J. Appl. Crystallogr.* **1976**, *9*, 403−406.
(38) Singh, S. K.; Neek Amal, M.; Costamagna, S.; Peeters, F. M. Thermomechanical Properties of a Single Hexagonal Boron Nitride Sheet. *Phys. Rev. B* **2013**, *87*, 184106.
(39) Okada, Y.; Tokumaru, Y. Precise Etermination of Lattice Parameter and Thermal Expansion Coefficient of Silicon between 300 and 1500 K. *J. Appl. Phys.* **1984**, *56*, 314−320.
(40) Atallah, T. L.; Wang, J.; Bosch, M.; Seo, D.; Burke, R. A.; Moneer, O.; Zhu, J.; Theibault, M.; Brus, L. E.; Hone, J.; Zhu, X. Electrostatic Screening of Charged Defects in Monolayer MoS_2. *J. 1. Phys. Chem. Lett.* **2017**, *8*, 2148−2152.
(41) Leconte, N.; Kim, H.; Kim, H.-J.; Ha, D. H.; Watanabe, K.; Taniguchi, T.; Jung, J.; Jung, S. Graphene bubbles and their role in graphene quantum transport. *Nanoscale* **2017**, *9*, 6041−6047.
(42) Mouri, S.; Miyauchi, Y.; Matsuda, K. Tunable Photoluminescence of Monolayer MoS_2 via Chemical Doping. *Nano Lett.* **2013**, *13*, 5944−5948.
(43) Martincová, J.; Otyepka, M.; Lazar, P. Is Single Layer MoS_2 Stable in the Air? *Chem. - Eur. J.* **2017**, *23*, 13233−13239.
(44) Gao, J.; Li, B.; Tan, J.; Chow, P.; Lu, T.-M.; Koratkar, N. Aging of Transition Metal Dichalcogenide Monolayers. *ACS Nano* **2016**, *10*, 2628−35.
(45) Liu, G.-B.; Shan, W.-Y.; Yao, Y.; Yao, W.; Xiao, D. Three-band tight-binding model for monolayers of group-VIB transition metal dichalcogenides. *Phys. Rev. B* **2013**, *88*, 085433.
(46) Kormányos, A.; Burkard, G.; Gmitra, M.; Fabian, J.; Zólyomi, V.; Drummond, N. D.; Fal'ko, V. k·p theory for two-dimensional transition metal dichalcogenide semiconductors. *2D Mater.* **2015**, *2*, 022001.
(47) Echeverry, J. P.; Urbaszek, B.; Amand, T.; Marie, X.; Gerber, I. C. Splitting between bright and dark excitons in transition metal dichalcogenide monolayers. *Phys. Rev. B* **2016**, *93*, 121107.
(48) McCreary, K. M.; Hanbicki, A. T.; Singh, S.; Kawakami, R. K.; Jernigan, G. G.; Ishigami, M.; Ng, A.; Brintlinger, T. H.; Stroud, R. M.; Jonker, B. T. The Effect of Preparation Conditions on Raman and Photoluminescence of Monolayer WS_2. *Sci. Rep.* **2016**, *6*, 35154.
(49) Florian, M.; Hartmann, M.; Steinhoff, A.; Klein, J.; Holleitner, A. W.; Finley, J. J.; Wehling, T. O.; Kaniber, M.; Gies, C. The Dielectric Impact of Layer Distances on Exciton and Trion Binding Energies in van der Waals Heterostructures. *Nano Lett.* **2018**, *18*, 2725−2732.
(50) Lloyd, D.; Liu, X.; Christopher, J. W.; Cantley, L.; Wadehra, A.; Kim, B. L.; Goldberg, B. B.; Swan, A. K.; Bunch, J. S. Band Gap Engineering with Ultralarge Biaxial Strains in Suspended Monolayer MoS_2. *Nano Lett.* **2016**, *16*, 5836−5841.
(51) Fu, Y.; He, D.; He, J.; Bian, A.; Zhang, L.; Liu, S.; Wang, Y.; Zhao, H. Effect of Dielectric Environment on Excitonic Dynamics in Monolayer WS_2. *Advanced Materials Interfaces* **2019**, *6*, 1901307.

https://doi.org/10.1021/acsami.1c18991
ACS Appl. Mater. Interfaces 2022, 14, 2255−2262